We are IntechOpen, the world's leading publisher of Open Access books
Built by scientists, for scientists

6,900
Open access books available

186,000
International authors and editors

200M
Downloads

Our authors are among the

154
Countries delivered to

TOP 1%
most cited scientists

12.2%
Contributors from top 500 universities

CLARIVATE ANALYTICS

BOOK CITATION INDEX

INDEXED

WEB OF SCIENCE™

Selection of our books indexed in the Book Citation Index
in Web of Science™ Core Collection (BKCI)

Interested in publishing with us?
Contact book.department@intechopen.com

Numbers displayed above are based on latest data collected.
For more information visit www.intechopen.com

A New Control Strategy to Integrate Flow Batteries into AC Micro-Grids with High Wind Power Penetration

Leonardo Javier Ontiveros,
Gastón Orlando Suvire and Pedro Enrique Mercado

Additional information is available at the end of the chapter

Abstract

The penetration of wind generation into AC micro-grids (MGs) has been increasing in recent years. Wind generation is uncontrollable, variable in nature, and uncertain. If the penetration level is high, the random variations of the wind power generation could cause problems for MGs to maintain the nominal system frequency. A typical solution is to employ energy storage systems (ESS) into the MG in order to compensate the wind power fluctuations. In this chapter, the use of a vanadium redox flow battery (VRFB) coupled with a power conditioning system (PCS) is suggested to enhance the frequency stability of a MG with high wind power penetration. A new control system is developed for the PCS/VRFB. The control system performs the load leveling of the wind generation and carries out the primary and secondary frequency control of the MG. Dynamic simulations of the proposed device are performed and demonstrate that the new control system improves the transient responses of the PCS/VRFB and the MG, during minor and/or severe disturbances.

Keywords: wind generation, AC micro-grids, energy storage, vanadium redox flow battery, power conditioning system, control system, frequency stability

1. Introduction

Wind generation is one of the most used renewable energy resources in AC micro-grids (MGs). Last year, wind power generation grew by 17% [1]. The incorporation of wind farms into the power system introduces new challenges to the operation, control, and planning of MGs, both for short-term intervals (seconds to minutes) and long-term intervals (minutes to hours). This is produced by the random variations of the wind resource. As a result, wind farms cannot be dispatched in the traditional sense. Conventional power plants struggle to meet variable demand, while wind turbines not. This leads to more problems into the MG. These problems

increase when the penetration level is high, compromising the operation security and reliability of MGs [2, 3]. The traditional solution is to increase the reserve generation of conventional power plants, what causes a noneconomic dispatch. Other solutions are provided by the manufacturers of wind turbines, employing both the speed and the pitch control systems as methods of supplying power reserve for frequency support and power generation smoothing on variable-speed wind turbines [4–6]. However, these solutions depend on the operating point of the wind turbine and are less efficient than that provided by an energy storage system (ESS). The output power of wind generators is reduced in order to gain controllability, but sacrificing a part of the free wind energy and consequently increasing the more expensive output power of conventional generators to cover the same power demand.

ESS can be employed in order to improve the frequency stability of MGs with high wind power penetration. In this sense, several previous works focus on the problems caused by wind generation and how an ESS can effectively solve them [7–11]. However, these solutions are limited according to the amount of energy stored by the used ESS. Nowadays, a promising low-cost, large stationary advanced ESS for these applications is the vanadium redox flow battery (VRFB), which presents high-speed response and overload capacity characteristics [12–14].

The incorporation of the VRFB into MGs requires a power conditioning system (PCS) and appropriate control strategy to manage the power flow between the VRFB and the utility system [12, 13]. Many solutions using PCS for long-term ESS have been proposed and listed in Ref. [15], a bidirectional single-phase inverter with a DC/AC converter connects a battery energy storage system (BESS) to the AC grid. Additionally, an integrated nonlinear control strategy is proposed both to control converters and to manage the power flow direction between the BESS and a stiff grid. In Ref. [16], a DC-DC converter system is presented based on an input-series/output-parallel dual active bridge structure, in a full modular design. The proposed converter is dedicated to interface a DC voltage network with a battery-based energy storage device. In Ref. [17], a non-isolated online uninterruptible power supply (UPS) is presented. The proposed system consists of bridgeless boost rectifier, battery charger/discharger, and an inverter. For the inverter, a new control method is developed, which regulates the output voltage for both linear and nonlinear loads. In Ref. [18], a grid-connected hybrid PV-wind-battery system with a bidirectional DC/DC chopper is presented. The control strategy manages the power flow from different sources, provides generation reserve to the grid, charges the battery, and satisfies the load demand. The work presented in Ref. [19] proposes a PCS for zinc-bromine (Zn-Br) flow battery-based energy storage system. The PCS consists of four DC-DC converters, one DC-AC inverter, and a battery management system. The battery control strategy including the PCS and the stripping operation is described to perform the charging and the discharging of the flow battery in steady state.

The proposals mentioned above offer practical solutions to connect the VRFB to the AC network. However, much less has been done particularly on the utilization of the VRFB in emerging grid-interactive AC MGs, although major benefits apply [20]. Moreover, none of the aforementioned work has discussed strategies to stabilize the active power flow of wind farms employing long-term ESS and to contribute to the frequency control when faults occur in the electrical system.

Based on the previous discussion, this work employs the PCS presented by the same authors in Ref. [21] and develops a new control strategy, which performs the load leveling of the wind farm and the frequency regulation of the MG. The PCS consists of a 12-pulse thyristor converter with commutated capacitors (TCCC). A TCCC is a fast-response, solid-state power compensator that provides active power control at the point of connection to the MG for power quality improvements. This characteristic enables the TCCC/VRFB (1) to mitigate short-term and mid-term power fluctuations of wind turbines, (2) to correct frequency fluctuations of the MG, and (3) to provide the reserve generation required during minor and severe disturbances.

With the aim of demonstrating the validity of the three statements of the preceding paragraph, a model of a TCCC/VRFB device is presented with all its components represented in detail. Moreover, a new control design for this device is developed; this is the main contribution of this work. The control system implements a new approach based on multilevel control technique. To mitigate wind power fluctuations, the control includes a load-leveling compensator block. In addition, the control system incorporates a frequency regulator, which performs the primary and secondary frequency control of the MG (PFC and SFC, respectively). Validation of models and control schemes is carried out through simulations by using SimPowerSystems of Simulink/MATLAB™.

Considering the aspects mentioned above, this work is organized as follows: the VRFB and the proposed compensator are presented in Section 2. The new control system of the TCCC/VRFB is developed in Section 3. The model of the MG is presented in Section 4. Simulation tests are performed in Section 5. Finally, the conclusions are presented in Section 6.

2. The TCCC/VRFB compensator

The TCCC/VRFB compensator is composed of the vanadium redox flow battery and the thyristor converter with commutated capacitors; both of them are explained below.

2.1. Vanadium redox flow battery

The VRFB is an electrochemical ESS which consists of two electrolytes stored in two separate tanks. The electrolytes are formed by sulfuric acid with active vanadium species in different oxidation states: V4/V5 redox couple (catholyte) and V2/V3 redox couple (anolyte). These liquids circulate through the cell stack by pumps. The stack consists of several cells, each of which contains two half-cells that are separated by a proton exchange membrane (PEM). The electrochemical reactions take place in the half-cells, and then inert carbon felt polymer composite electrodes are employed in order to charge or discharge the battery through an external DC current. The general scheme of the VRFB is represented in **Figure 1(a)**.

The half-cell of the VRFB performs two simultaneous chemical reactions; these reactions occur on both sides of the membrane as shown in **Figure 1(b)**. During the charge process, the positive electrolyte (catholyte) delivers electrons to the negative electrolyte (anolyte) through
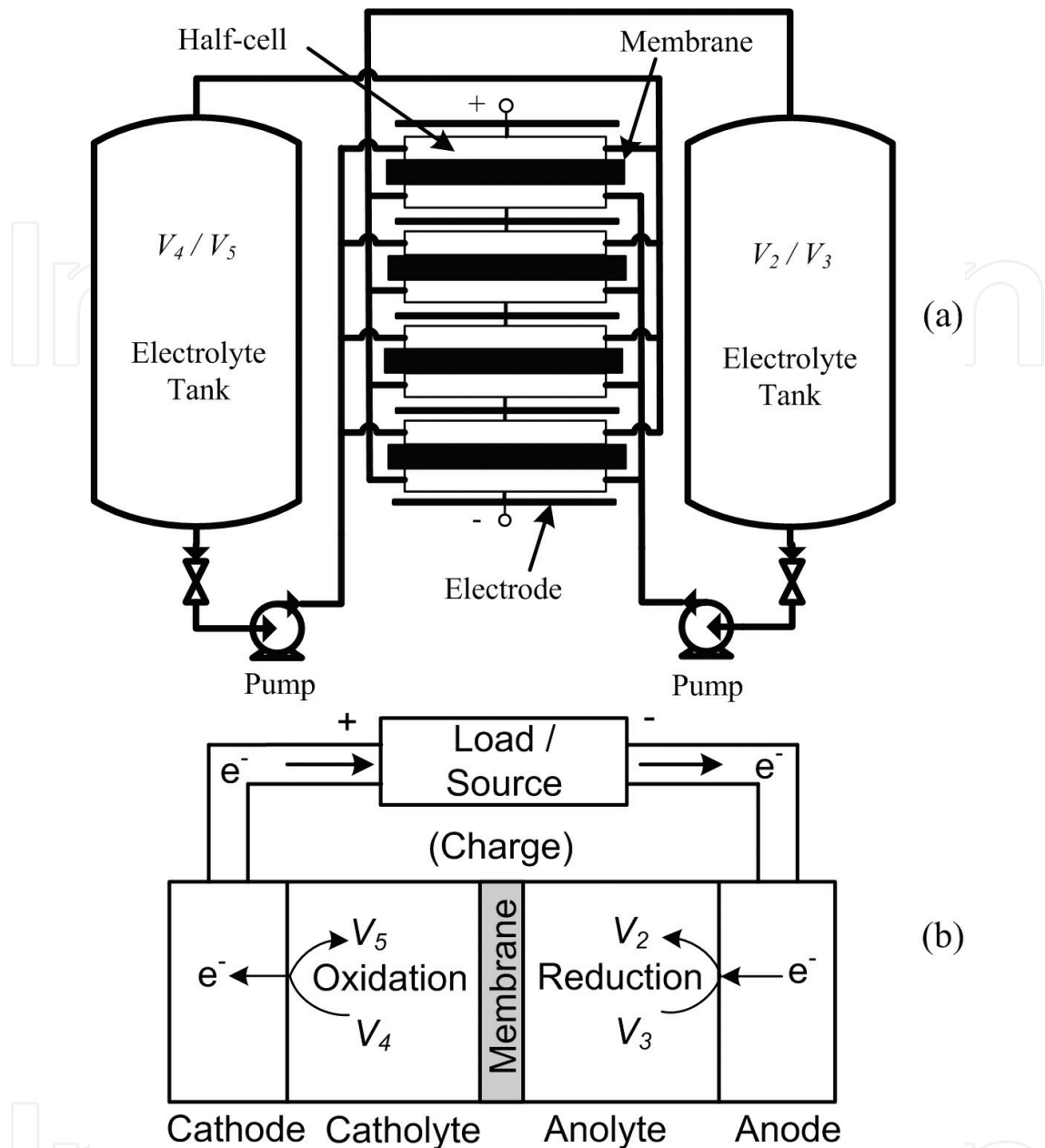
Figure 1. Vanadium redox flow battery: (a) general scheme and (b) chemical reactions.

the external circuit. Therefore, the oxidation occurs in the catholyte, and the reduction occurs in the anolyte. During the discharge process, the flow of electrons is reversed; the oxidation takes place in the anolyte and the reduction in the catholyte.

The battery produces a nominal cell potential of approximately 1.25 V. By connecting many cells into a "stack," the terminal voltage is obtained. The current density through the cell and the stack voltage establish the power available, while the supply of charged electrolyte to the stack establishes the energy available. So, the rated power and the energy stored can be upgraded by increasing or decreasing the stack and the electrolyte tank, respectively [22–24].

2.2. Model of the VRFB

The VRFB model is composed by the stack model and the mechanical model, as shown in **Figure 2**. The complete model of the VRFB was developed in Ref. [22]. The stack model calculates the state of charge (SOC) of the electrolyte and the terminal stack voltage (U_{stack}). These values depend on the initial SOC and the stack current (I_{stack}). On the other hand, the mechanical model calculates the hydraulic losses caused by the electrolyte flow rate (Q). This flow rate is produced by two DC machines that drive the pumps. Therefore, the stack current is calculated from the difference between the terminal VRFB current (I_{VRFB}) and the pump current consumption (I_{pump}).

2.2.1. VRFB stack model

The proposed electrochemical model of the VRFB calculates two gains in order to obtain the stack voltage U_{stack} and the effective current I_{ef}. These parameters are the voltage and current gains (K_v, K_c), and they are obtained by solving (Eqs. (1) and (2)). Note that K_c and K_v gains depend on the stack current, the experimental efficiency curves (**Figure 3**) [23, 24], and the operating condition (charge or discharge):

$$K_{c,charge} = \eta_c K_{c,disch} = \eta_c \frac{(1+\eta_v)}{(1+\eta_e)} \tag{1}$$

$$K_{v,charge} = \frac{K_{v,disch}}{\eta_v} = \frac{(1+\eta_c)}{(1+\eta_e)} \tag{2}$$
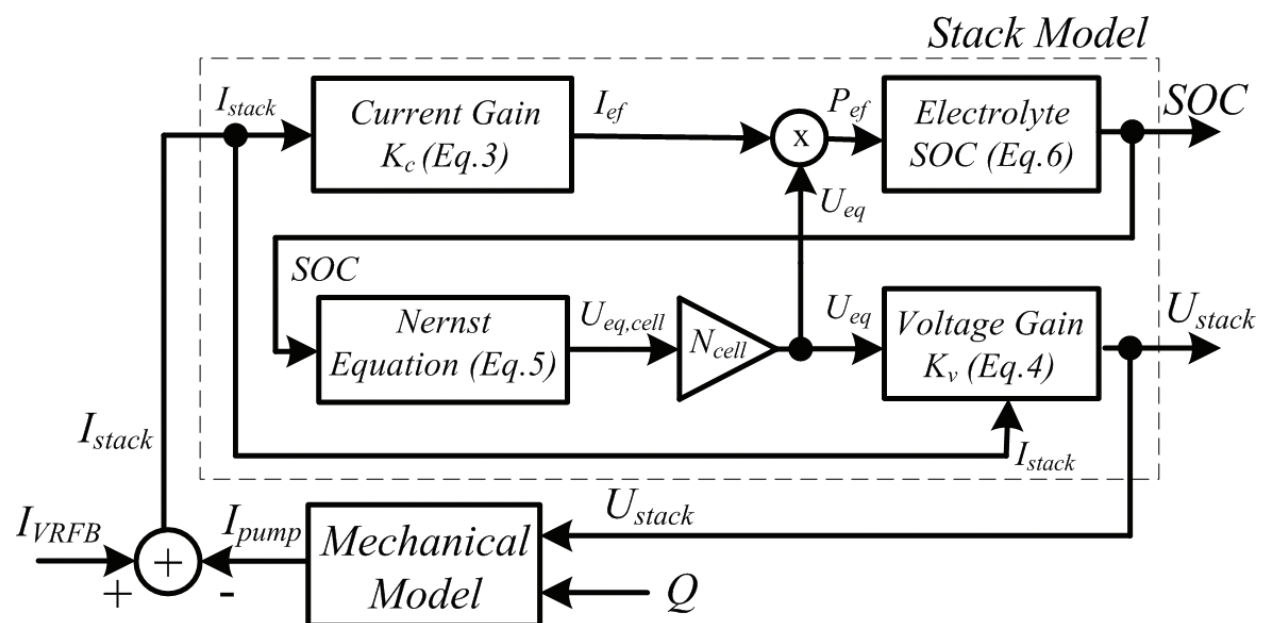

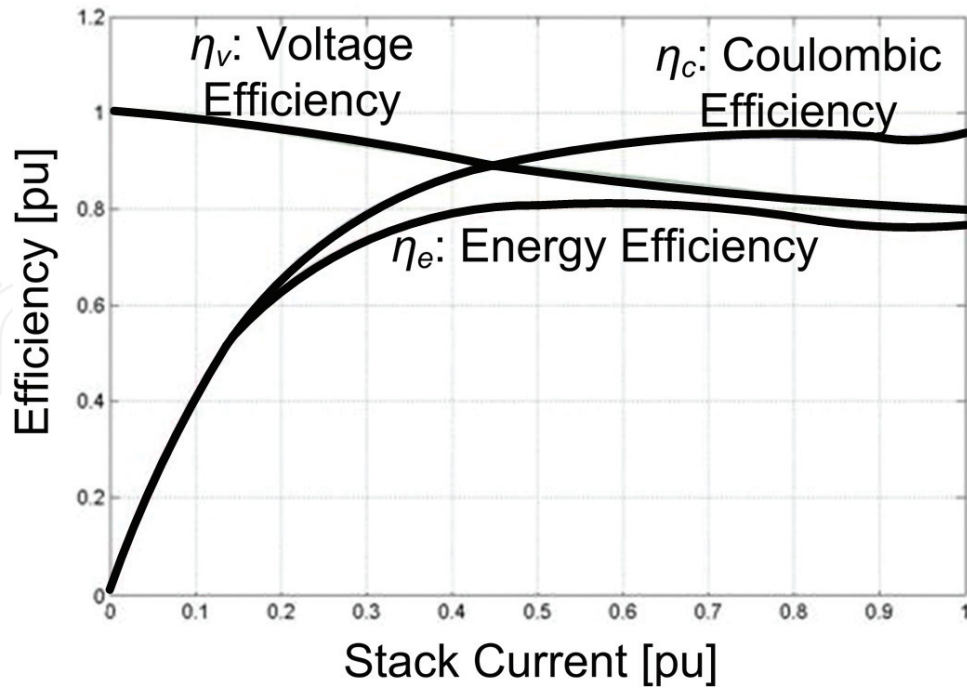**Figure 2.** Mathematic model of the VRFB.

Figure 3. Voltage, coulombic, and energy efficiencies of the VRFB stack.

The effective stack current and the terminal stack voltage are obtained with (Eqs. (3) and (4)):

$$I_{ef} = K_c I_{stack} \tag{3}$$

$$U_{stack} = K_v U_{eq} \tag{4}$$

The equilibrium voltage (U_{eq}) can be calculated employing the Nernst equation (Eq. (5)) [25–28]:

$$U_{eq} = N_{cell} \left[U_0 + \frac{2RT}{F} \ln\left(\frac{SOC}{1 - SOC}\right) \right] \tag{5}$$

where U_0 is the internal cell voltage when the SOC is 0.5 pu, N_{cell} is the number of cells in series connection, F is the Faraday constant, T is the absolute temperature, and R is the gas constant. The value of SOC depends on the effective stack power, the storage capacity (E_{max}), and the initial conditions (SOC_0) (Eq. (6)) [29]:

$$SOC = SOC_0 + \int \frac{-U_{eq} I_{ef}}{E_{max}} dt \tag{6}$$

2.2.2. Mechanical model

The mechanical model of the VRFB system is developed in Ref. [30]. This model consists of an analytical part and a numerical part. The analytical part models the pipes, bends, valves, tanks, and pumps. The numerical part describes the more complex stack hydraulic circuit. In addition to the mechanical model, in this work it is suggested to incorporate the equivalent DC

current consumption of the pumps (I_{pump}). Therefore, the value of I_{pump} represents the mechanical losses of the VRFB system (Eq. (7)):

$$I_{pump} = \frac{P_{2pumps}}{U_{stack}} \tag{7}$$

2.3. Thyristor converter with commutated capacitors

A DC/AC bidirectional converter is required in order to connect the VRFB to the MG. In this regard, a 12-pulse thyristor converter with commutated capacitors on the AC side (TCCC) is proposed for controlling the active power flow of the VRFB [21]. The TCCC operates as a current source. Therefore, the polarization voltage of the VRFB stack determines the voltage at the DC bus (V_{conv}). As a result, the connection between the VRFB and the TCCC does not require a DC/DC chopper. **Figure 4** shows the proposed PCS unit for the VRFB system.

The most important aspects of the proposed PCS are:

- The converter can only draw an inductive current from the MG.

- A valve cannot be turned off actively. Instead, the current through one valve has to be brought to zero by turning on another valve.

- The reactive power consumption of the converter decreased by the additional voltage provided by the capacitors C_{con}. This leads to a reduction of the risk of commutation failures.

The TCCC contains tuned filters to smooth the AC current harmonics of order $12n \pm 1$. Additionally, the reactive power required by the thyristor converter is provided by these filters. From **Figures 2** and **4**, the following equalities are obtained:
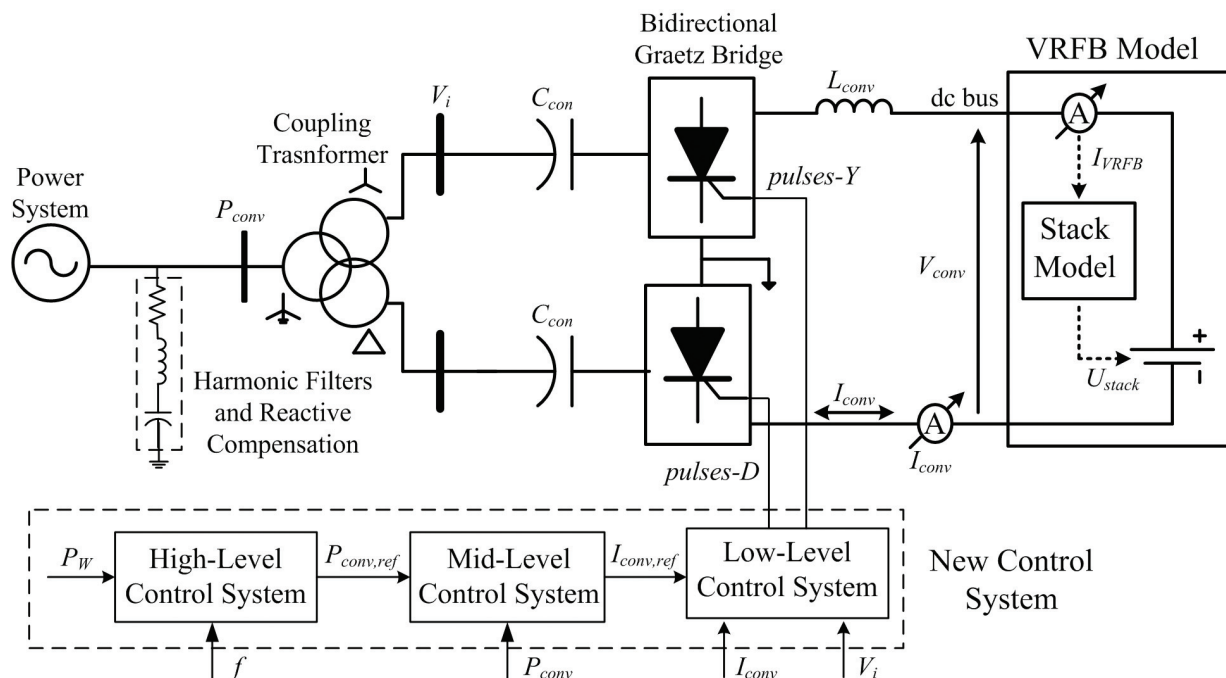

Figure 4. The proposed PCS unit (TCCC).

$$I_{VRFB} = I_{stack} + I_{pump} = I_{conv} \tag{8}$$

$$V_{conv} = U_{stack} \tag{9}$$

Eq. (8) shows that the VRFB terminal current is imposed by the converter current, whereas (Eq. (9)) demonstrates that the TCCC terminal voltage is the polarization voltage of the VRFB. The calculation of the TCCC current at the DC bus is obtained from Ref. [31]:

$$V_{conv} = b\frac{3}{\pi}\sqrt{2}V_{i,RMS}\cos\alpha - \frac{3}{\pi}(x_t - x_c)I_{conv} \tag{10}$$

where x_t and x_c are the transformer and capacitor (C_{con}) reactance, respectively; $V_{i,RMS}$ is the RMS voltage of the TCCC at the AC bus; α is the firing angle of the converter; and b is a sign factor which determines the operation mode of the converter: +1 for rectifier operation mode ($0 < \alpha < \pi/2$) and -1 for inverter operation mode ($\pi/2 < \alpha < \pi$). The DC current at VRFB terminals is obtained solving (Eqs. (8))–(10)):

$$I_{VRFB} = \frac{b}{(x_t - x_c)}\left(\sqrt{2}V_{i,RMS}\cos\alpha - \frac{\pi}{3}U_{stack}\right) \tag{11}$$

Considering constant values of $V_{i,RMS}$ and U_{stack}, I_{VRFB} decreases when α increases, while in rectifier operation mode, and I_{VRFB} increases when α increases during inverter operation mode.

3. Control system of the TCCC

In this section a new multilevel control system has been developed for the TCCC unit; this control system has its own control objectives for each hierarchical control level [9]. The proposed multilevel control system is shown in **Figure 5**, which is composed of three parts: a low-level control system, a mid-level control system, and a high-level control system.

The low-level and mid-level control systems are fully developed in Ref. [21], whereas the high-level control system (left side of **Figure 5**) is presented below which represents the main contribution of this work.
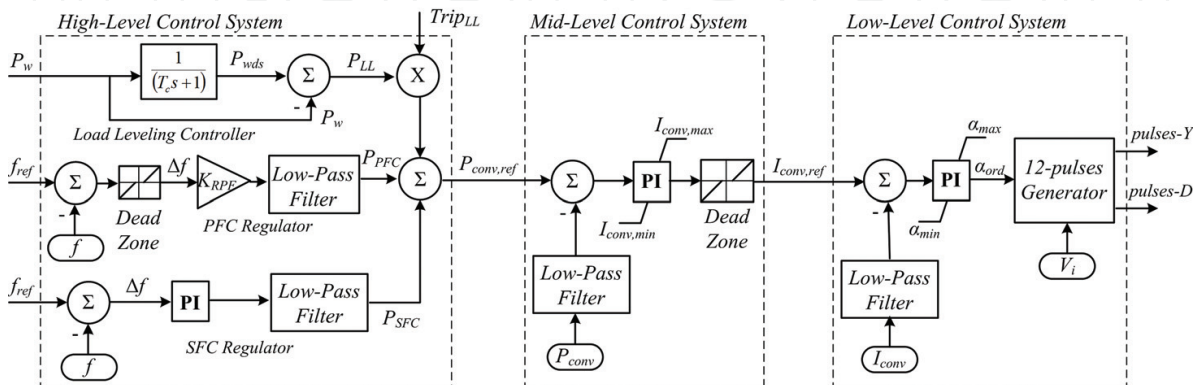

Figure 5. New control system of the TCCC.

3.1. High-level control system

The high-level control system is responsible for determining the active power exchange between the TCCC and the utility system. The goal of the control algorithm is to perform the load leveling of the wind generation and to provide the generation reserve required for frequency regulation. This controller is composed of three parallel control loops: the load-leveling controller, the PFC regulator, and the SFC regulator. The aim of the load-leveling controller is to eliminate the turbulent component of the wind power (P_w). So, a first-order filter with a cutoff frequency at one cycle/hour is employed in order to obtain the diurnal and synoptic component of the wind power (P_{wds}) [32, 33]. The difference between P_{wds} and P_w is the compensation power P_{LL} that must be supplied or absorbed by the TCCC/VRFB unit. The load-leveling controller is always active, thus allowing for improvement in the power quality of the electric utility grid with wind generators.

On the contrary, the PFC and SFC regulators are only active when significant frequency deviations arise, contributing to recover the rated system frequency and thus improving the grid security. These controllers are in charge of minimizing the magnitude and duration of system disturbances by damping power oscillations. The purpose of this is to keep the system frequency between minimum and maximum levels during the transient dynamics. This is accomplished by measuring the frequency error Δf, which is proportional to the rate of change of the generator angle $d\delta/dt$ involved and consequently directly represents the power oscillation of the system. The value of Δf enters to proportional and proportional-integral (PI) control schemes, in order to calculate the generation reserve required to perform the PFC and SFC (P_{PFC}, P_{SFC}), respectively. In the PFC regulator, a dead-band block is incorporated within the control loop with the purpose of managing the participation of the TCCC/VRFB in the frequency control of the utility system. The low-pass filters are employed to eliminate the noise signal. Finally, the three components are added together to obtain the converter reference power $P_{conv,ref}$.

3.2. Mid-level and low-level control system

The mid-level control and the low-level control systems operate the TCCC as a controlled current source. The control algorithm is shown in **Figure 5**. The mid-level control system calculates the DC reference current ($I_{conv,ref}$) by comparing the reference power $P_{conv,ref}$ with the converter power (P_{conv}). The nonlinearity of the converter at low current is eliminated by a dead zone block. In the low-level control system, the reference firing angle (α_{ord}) for the thyristors is calculated from the reference current $I_{conv,ref}$ and the converter current (I_{conv}). Then, the value of α_{ord} enters to a 12-pulse generator in order to produce the firing pulses for the TCCC [31, 34].

4. Micro-grid model

A typical MG model shown in **Figure 6** is used for simulation studies; the SimPowerSystems® package of the MATLAB/Simulink software is employed to carry out the simulations. This model system is composed of a 132-kV-bulk power system (represented as an infinite AC bus)
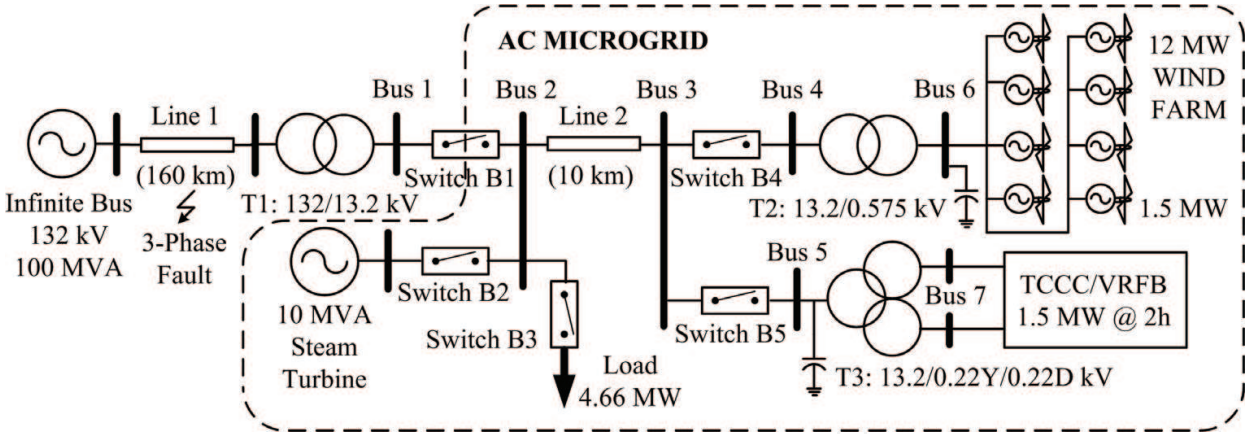
Figure 6. Single-line diagram of the test power system with an AC micro-grid including wind generation and the TCCC/VRFB system.
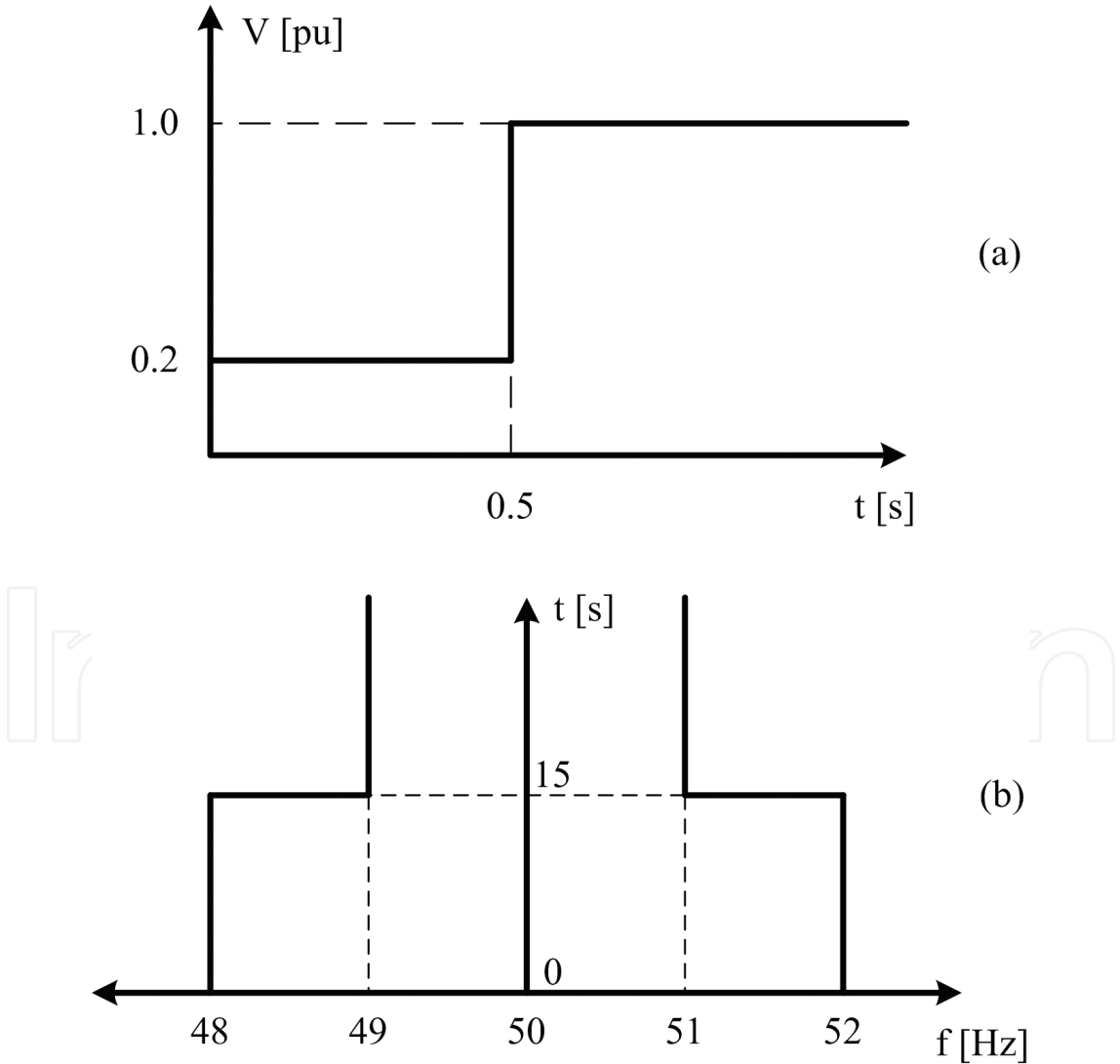

Figure 7. Capability curves of the wind farm: (a) voltage curve and (b) frequency curve.

connected to a 13.2 kV MG through a 160 km transmission line. The MG is composed of a 10 MVA steam turbine, a constant load, a 12 MW wind farm composed of eight double-fed induction generator (DFIG) wind turbines, and a 1.5 MW TCCC/VRFB unit. The energy and power ratings of the TCCC/VRFB unit are determined according to Refs. [35, 36] and proved through the simulations presented in Section V. The mathematical models of the TCCC and the steam turbine are detailed in the Appendix, and the wind farm model is developed in Refs. [37, 38].

The wind farm protection system is represented in **Figure 7**, which illustrates the voltage and frequency capability curves in **Figure 7(a) and (b)**, respectively. The protection system disconnects the wind farm when the terminal voltage is less than 0.2 pu during 0.5 s. On the other hand, frequency oscillations can also trip the wind farm. If the frequency of the MG is in the 49–48 or 51–52 Hz range during 15 s at least, the wind farm is switched off. If the frequency is lower than 48 Hz or higher than 52 Hz, the wind farm is instantaneously disconnected. The wind farm operates normally when the frequency of the MG is in the range of 49–51 Hz.

5. Simulation results

The frequency stability of the proposed MG is evaluated through simple events that impose high demands on dynamic response of the steam turbine and the TCCC/VRFB unit. In this regard, two case studies are considered. Case 1 evaluates the post-fault frequency stability of the MG when it is transmitting electric power to the 132 kV network. Case 2 examines the postfault frequency stability of the MG when it is importing electric power from the bulk power system. In addition to the frequency stability analysis, Case 3 evaluates the quality power supply during the isolated operation of the MG. The under-frequency load shedding system, which could help in maintaining the frequency drop after contingencies within acceptable values, is not considered in all the cases aiming at highlighting the benefits of the proposed solution.

5.1. Case 1: unexpected disconnection of the MG during energy exportation

In this case, the frequency stability of the system is analyzed when an unexpected single-phase fault occurs at Line 1. In consequence, switch B1 opens 0.1 s after the occurrence of the event, causing the isolated operation mode of the MG. When the fault occurs at $t = 150$ s, the steam turbine and the wind farm are generating 9.5 and 3 MW, respectively. The load is 11 MW, so the power imbalance is 1.5 MW approximately.

Figure 8(a) shows the frequency deviation of the MG. Since the power generation is higher than the load, the frequency increases after the fault. When the control strategy developed in Ref. [21] is employed (previous control strategy), the frequency reaches the value of 52 Hz at $t = 152.9$ s; at this instant the wind farm switches off due to over-frequency. After that, the load is higher than the power generation, hence the system frequency decreases. The steam turbine switches off at $t = 158.8$ s due to under-frequency. Therefore, the MG collapses due to the lack of generation. A similar situation occurs when the new control strategy is applied and the

rated power of the TCCC/VRFB is 1.0 MW. If the rated power of the TCCC/VRFB is 1.5 MW at least and the new control strategy is activated, the frequency reaches the value of 50.89 Hz at $t = 153.4$ s; after that the MG recovers the nominal value of the frequency (50 Hz).

Owing to the proportional characteristic of the PFC controller, the system frequency presents a steady-state error after the fault. In order to eliminate this error, the SFC controller participates in the frequency regulation. The steam turbine and the TCCC/VRFB compensator operate under this control scheme. These units restore the frequency after 70 s (**Figure 8(a)**).

The dynamic performance of the MG is represented in **Figure 8(b)–(d)**. After the fault at $t = 150$ s, the short-term reserve generation is activated in order to compensate the power unbalance of the MG. Since the power generation is higher than the load, the active power outputs of the steam turbine and the TCCC/VRFB unit decrease according to **Figure 8(b)** and **(d)**, respectively. According to **Figure 8(d)**, when the 1.0 MW TCCC/VRFB is operating in the saturation region, there is no frequency control. Hence, the wind farm and the steam turbine switch off at $t = 169$ and 175 s, respectively. The incorporation of the 1.5 MW TCCC/VRFB compensator and the proposed control strategy avoid the collapse of the MG, in accordance with **Figure 8(a)**.

5.2. Case 2: unexpected disconnection of the MG during energy importation

In this simulation, the frequency stability of the power system is analyzed when a fault occurs at line 1, whereas the MG is importing energy from the bulk power system. An unexpected single-phase fault occurs at $t = 150$ s; in a consequence switch B1 opens 0.1 s after the occurrence of the fault, causing the MG to operate in isolated mode. When the fault occurs, the
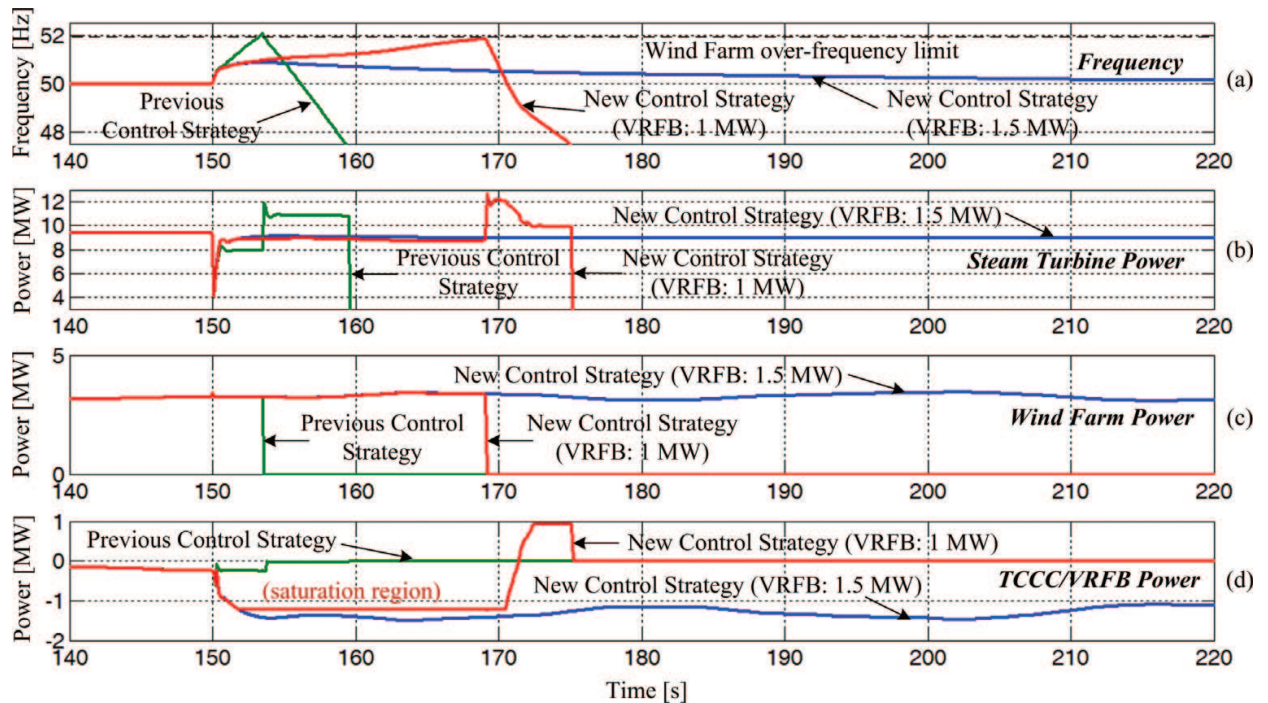

Figure 8. Dynamic response of the MG in Case 1: (a) frequency deviation, (b) steam turbine power, (c) wind farm active power, and (d) TCCC/VRFB active power.
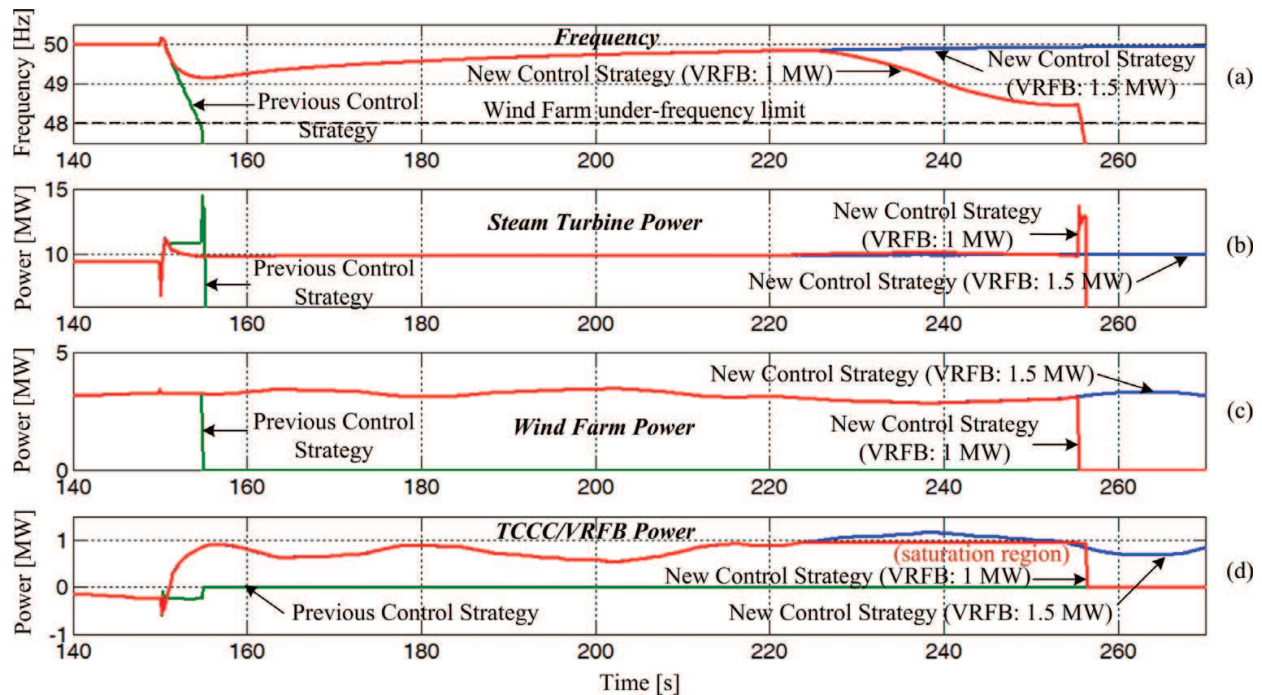
Figure 9. Dynamic response of the MG in Case 2: (a) frequency deviation, (b) steam turbine power, (c) wind farm active power, and (d) TCCC/VRFB active power.

steam turbine and the wind farm are generating 9.5 and 3 MW, respectively. The load is 14 MW, so the power unbalance is −1.5 MW approximately.

The frequency deviation of the MG is shown in **Figure 9(a)**. In this case, the load is higher than the power generation, so the frequency decreases after the fault. When the previous control strategy is employed, the frequency reaches the value of 48 Hz at $t = 155.6$ s; at this instant the wind farm switches off due to under-frequency. In a consequence, the system collapses owing to the lack of generation at $t = 156$ s. If the new control strategy is activated and the rated power of the TCCC/VRFB is at least 1.5 MW, the frequency reaches the value of 49.15 Hz at $t = 155.4$ s; after that the frequency asymptotically recovers its nominal value.

The dynamic response of the MG is shown in **Figure 9(b)–(d)**. Because the load is higher than the power generation, the short-term generation reserve is activated in order to compensate the power unbalance. Therefore, the steam turbine and the TCCC/VRFB increase the power output according to **Figure 9(b)** and **(d)**, respectively. Similarly in the previous case, when the 1.0 MW TCCC/VRFB is operating in the saturation region, there is no frequency control. Hence, the wind farm and the steam turbine switch off at $t = 256.2$ s. The incorporation of the 1.5 MW TCCC/VRFB unit and the proposed control strategy avoid the collapse of the MG as in the previous case (**Figure 9(a)**).

5.3. Case 3: isolated operation of the MG

Maintaining the voltage and frequency within certain limits in a MG is a basic operational requirement as many loads may be very sensitive to voltage and frequency deviations. Increasing wind penetration in the MG may lead to stability problems or produce unwanted voltage

and frequency oscillation in isolated systems [2–4]. Bearing these aspects in mind, the dynamic performance of the MG is evaluated during the isolated operation. The operation conditions are as follows: the steam turbine is generating 4 MW (minimum operating power), the average wind farm active power is 3 MW, and the constant load is 7 MW. Therefore, the wind penetration is approximately 43%.

Figure 10(a) shows the frequency of the MG by considering two cases: with and without energy storage. When the TCCC/VRFB unit is not employed, the steam turbine presents problems in establishing the nominal value of the frequency as a result of random variations in wind power. When the TCCC/VRFB is used, the frequency deviations are less than 0.01 Hz approximately, enhancing the power quality supply of the MG.

Figure 10(b) shows the power output of the steam turbine and the wind farm. When the TCCC/VRFB unit is not employed, the steam turbine operates below the minimum operating power (4 MW) during several intervals. This situation is avoided when the TCCC/VRFB performs the load leveling of the wind power generation (**Figure 10(c)**), causing a reduction of the mechanical stress of the steam turbine. **Figure 10(d)** demonstrates that the steam turbine and the wind farm can control effectively the voltage of buses 2 and 3, respectively.

These simulations show that the TCCC/VRFB unit and the new control system enhance the dynamic response of MGs which incorporate wind generation, by performing the load leveling of wind turbines and carrying out the frequency regulation of the MG. It is important to notice that the DFIG wind farm and the TCCC/VRFB unit complement each other; the reactive power fluctuations generated by the TCCC are compensated by the wind farm, whereas the fluctuations of the wind power generation are smoothed by the TCCC/VRFB unit.
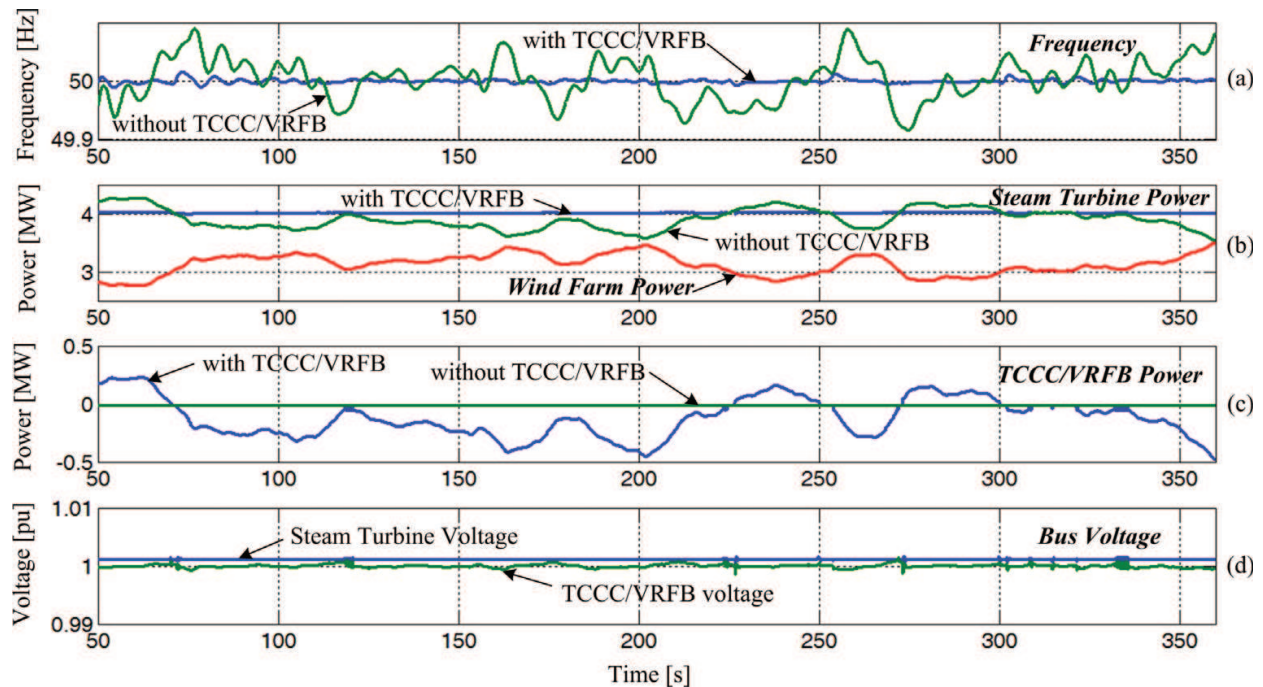

Figure 10. Dynamic response of the MG in Case 3: (a) frequency deviation, (b) steam turbine/wind farm power, (c) TCCC/VRFB active power, and (d) bus voltage.

6. Conclusions

This work proposes a new control strategy for the TCCC/VRFB unit for enhancing the transient response of a MG with high wind power penetration. The control strategy has been implemented with a multilevel control topology. The high-level control system, which is the core of the contribution, sets the power that exchanges the TCCC/VRFB with the MG. The aims of this power flow are (1) to smooth the active power generated by a DFIG wind farm and (2) to provide the generation reserve required for PFC and SFC. The model aspects of the VRFB and the TCCC unit are also presented.

From the results obtained, it can be concluded that the developed control algorithms work satisfactorily. The TCCC/VRFB unit, with the operation of the load-leveling controller, effectively compensates the active power fluctuations from a wind farm. The complete system (wind farm plus TCCC/VRFB) generates a smoother power response than that of the system without the TCCC/VRFB. Moreover, the complete control system, now with the operation of the PFC and SFC controllers, also contributes to the recovery of the frequency when severe disturbances occur in the MG. Therefore, the incorporation of the TCCC/VRFB compensator and its new control system improves the integration of wind turbines into AC MGs.

Acknowledgements

Appendix

TCCC model

The TCCC is composed of two bidirectional Graetz bridges, a coupling transformer with three windings, harmonic filters, and passive elements, as shown in **Figure 4**. The model of the thyristor is composed of an inductor L_{tyr}, a resistor R_{tyr}, and a DC voltage source that represents the forward voltage V_{ft}. These components are connected in series. A logical signal that depends on the gate signal g, the current I_{AK}, and the voltage V_{AK} controls the switch. A series R_{snub}-C_{snub} snubber circuit is connected in parallel with the thyristor model. **Figure 11(b)** shows the static VI characteristic of the model. The thyristor and TCCC parameters are shown in **Tables 1** and **2**.

Steam turbine model

According to **Figure 12**, the steam turbine model is composed of a four-stage steam turbine, a shaft with up to four masses, a speed governing system, and an automatic generation control (AGC) system. The speed governing system is composed of a servomotor that regulates the
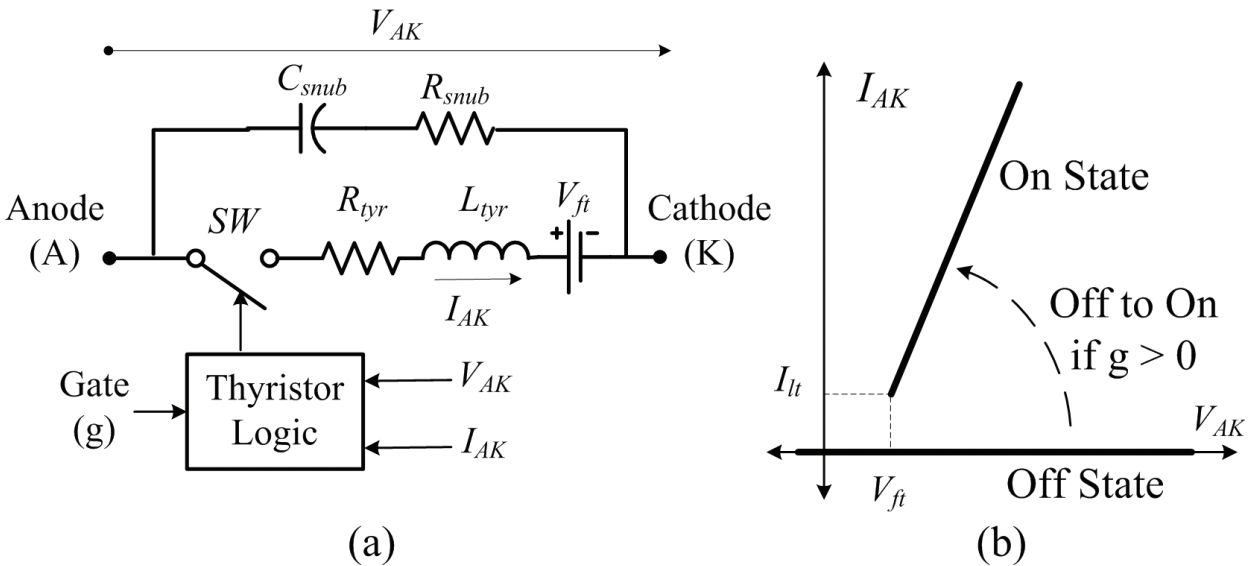
Figure 11. (a) Thyristor model and (b) static VI characteristic of the thyristor.

R_{tyr} (mΩ)	L_{tyr} (mH)	V_{ft} (V)	C_{snub} (nF)	R_{snub} (Ω)
1	0	2	100	2000

Table 1. Thyristor parameters.

Harmonic	Harmonic filters			Converter	
	L_{filt} (mH)	R_{filt} (Ω)	C_{filt} (nF)	C_{con} (mF)	L_{conv} (mH)
11th	117.52	4.06	712.4	30	7
13th	84.14	3.43	712.4	–	–
23–25th	24.68	558.46	712.4	–	–

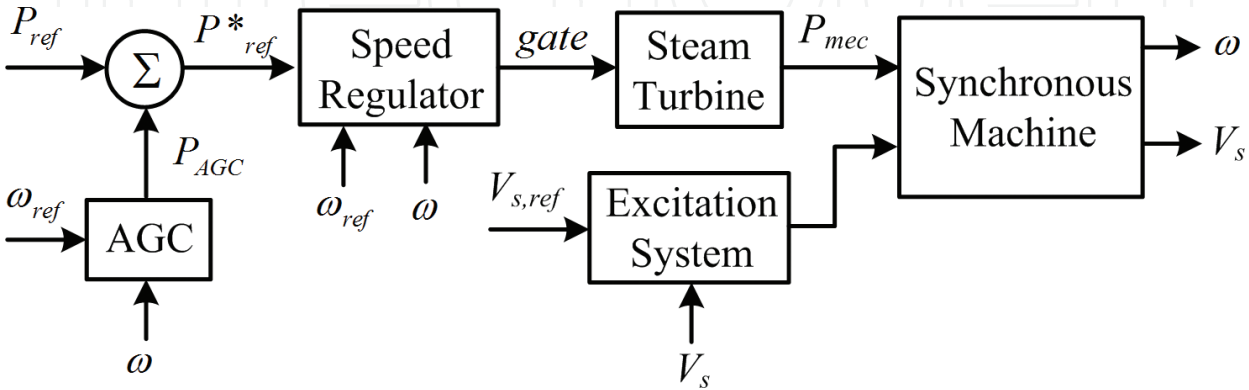**Table 2.** TCCC parameters.

Figure 12. Steam turbine model.

turbine valve, a proportional regulator, and a speed relay. A PI regulator performs the secondary frequency control at the AGC subsystem. In this work, the load variations of the steam turbine are less than 4%; therefore, the boiler pressure is assumed constant during the simulation time [39].

Author details

Leonardo Javier Ontiveros*, Gastón Orlando Suvire and Pedro Enrique Mercado

*Address all correspondence to: ontiveros@iee.unsj.edu.ar

National Scientific and Technical Research Council (CONICET), San Juan, Argentina

References

[1] World Wind Energy Association Website. www.wwindea.org [Internet]. June 2016. Available from: http://www.wwindea.org/the-world-sets-new-wind-installations-record-637-gw-new-capacity-in-2015/ [Accessed: June 2016]

[2] Chandra D, Grimaccia F, Kumari M, Sydulu M, Mussetta M. Transient stability analysis of power system with grid integration of wind generation. International Review of Electrical Engineering (IREE). 2015;**10**(3):442-448. DOI: 10.15866/iree.v10i3.6037

[3] Daneshi H, Srivastava A. Impact of battery energy storage on power system with high wind penetration. In: IEEE PES, editor. Transmition and Distribution Conference and Exposition T&D 2012; May 2012; Orlando, FL, USA. Orlando, FL, USA: IEEE PES; 2012. pp. 1-8

[4] Chakib R, Essadki A, Cherkaoui M. Participation of DFIG wind turbine controlled by active disturbance rejection control in primary frequency control. International Review of Electrical Engineering (IREE). 2016;**11**(2):183-192. DOI: 10.15866/iree.v11i2.8150

[5] Vestas Wind Systems Website. www.vestas.com [Internet]. June 2016. Available from: http://www.vestas.com [Accessed: June 2016]

[6] GE Enegy Website. www.ge-energy.com [Internet]. June 2016. Available from: http://www.ge-energy.com/products_and_services/products/ [Accessed: June 2016]

[7] Xu Q, Zang H, Shi L, Du P. Researches on power system low-frequency oscillations damping with FESS. International Review of Electrical Engineering (IREE). 2011;**6**(5):2537-2544. DOI: 10.1109/ICPST.2006.321886

[8] Gan C, Prayun W, Tan C, Shamshiri M. Design of a hybrid diesel/PV/wind/battery system in remote areas. International Review of Electrical Engineering (IREE). 2014;**9**(2):420-430

[9] Suvire G, Mercado P. Active power control of a flywheel energy storage system for wind energy applications. IET Renewable Power Generation. 2012;**6**(1):9-16. DOI: 10.1049/iet-rpg.2010.0155

[10] Molina M, Mercado P. Power flow stabilization and control of microgrid with wind generation by superconducting magnetic energy storage. IEEE Transactions on Power Electronics. 2011;**26**(3):910-922. DOI: 10.1109/TPEL.2010.2097609

[11] Suvire G, Molina M, Mercado P. Improving the integration of wind power generation into AC microgrids using flywheel energy storage. IEEE Transactions on Smart Grid. 2012;**3**(4):1945-1954. DOI: 10.1109/TSG.2012.2208769

[12] Mohamed M, Ahmad H, Seman M. State of the art of all-vanadium redox flow battery: A review on research prospects. International Review of Electrical Engineering (IREE). 2012;**7**(5):5610-5622

[13] Molina M, Suvire G, Ontiveros L, Mercado P. Emerging energy storage technologies in utility power systems: A technical insight. In: Rose M, editor. Energy Storage. 1st ed. New York: Nova Science Publishers Press; 2011. pp. 235-312

[14] Gerami Moghaddam I, Fallahi F. Self scheduling program for VRB energy storage system in competitive electricity market. International Review of Electrical Engineering (IREE). 2010;**5**(4):1707-1714. DOI: 10.1109/POWERCON.2010.5666037

[15] Braier C, Torres M, Muñoz J, Rivera M, Espinosa E, Acuña P. Bidirectional power flow control of a single-phase current-source grid-tie battery energy storage system. In: IEEE Latin America, editor. 2015 IEEE 24th International Symposium on Industrial Electronics (ISIE); June 2015; Búzios, Brazil. Búzios, Brazil: IEEE Latin America; 2015. pp. 1372-1377

[16] Barrade P, Rufer A. Control of a modular DC-DC converter dedicated to energy storage. In: Power Electronics and Applications (EPE'15 ECCE-Europe); September 2015; Geneva, Switzerland: IEEE; 2015. pp. 1-9

[17] Aamir M, Mekhilef S. online transformerless uninterruptible power supply (UPS) system with a smaller battery bank for low power applications. IEEE Transactions on Power Electronics. 2017;**32**(1):233-247. DOI: 10.1109/TPEL.2016.2537834

[18] Mangu B, Akshatha S, Suryanarayana D, Fernandes B. Grid-connected PV-wind-battery based multi-input transformer coupled bidirectional DC-DC converter for household applications. IEEE Journal of Emerging and Selected Topics in Power Electronics. 2016;**4**(3):1086-1095. DOI: 10.1109/JESTPE.2016.2544789

[19] Lim J, Lee S, Kang K, Cho Y, Choe G. A modular power conversion system for zinc-bromine flow battery based energy storage system. In: IEEE, editor. Future Energy Electronics Conference (IFEEC); November 2015; Taipei, Taiwan. Taiwan: IEEE; 2015. pp. 1-5

[20] Darabi A, Hosseina M, Gholami H. Vanadium redox flow battery control in flexible microgrids. International Review of Electrical Engineering (IREE). 2013;**8**(4):1341-1348

[21] Ontiveros L, Mercado P. Thyristor-based flexible AC transmission system for controlling the vanadium redox flow battery. IET Renewable Power Generation. 2013;**7**(3):201-209. DOI: 10.1049/iet-rpg.2012.0361

[22] Ontiveros L, Mercado P. Modeling of a vanadium redox flow battery for power system dynamic studies. International Journal of Hydrogen Energy. 2014;**39**(16):8720-8727. DOI: 10.1016/j.ijhydene.2013.12.042

[23] Wang G. Minimising output power fluctuation of large photovoltaic plant using vanadium redox battery storage. In: IET, editor. Power Electronics, Machines and Drives (IET/PEMD); March 2012; Bristol, UK. UK: IET; 2012. pp. 1-6

[24] Wang G. PV power plant using hybrid energy storage system with improved efficiency. In: IEEE, editor. Power Electronics for Distributed Generation Systems (IEEE/PEDG); June 2012; Aalborg, Denmark. Denmark: IEEE; 2012. pp. 808-813

[25] Chahwan J, Abbey C, Joos G. VRB modelling for the study of output terminal voltages, internal losses and performance. In: Electric Power Conference (EPC); October 2007; Montreal, Canada. Canada: IEEE; 2007. pp. 387-392

[26] Skyllas-Kazacos M, Menictas C. The vanadium redox battery for emergency back-up applications. In: Int. Telecommunications Energy Conference (INTELEC); October 1997; Melbourne, Australia. Australia: IEEE; 1997. pp. 463-471

[27] Mousa A. Chemical and electrochemical studies of V(III) and V(II) solutions in sulfuric acid solution for vanadium battery applications [thesis]. New South Wales, Australia: University of South Wales (UNSW); 2003. 632 p. Available from: http://handle.unsw.edu.au/1959.4/54984

[28] Tsuda I, Kurokawa K, Nozaki K. Development of intermittent redox flow battery for PV system. In: World Conference on Photovoltaic Energy Conversion (WCPEC); December 1994; Waikoloa, HI, USA. USA: IEEE; 1994. pp. 946-949

[29] Wang W. Grid-connected wind farm power control using VRB-based energy storage system. In: Energy Conversion Congress and Exposition (IEEE/ECCE); August 2010; Delft, Netherlands. Netherlands: IEEE; 2010. pp. 3772-3777

[30] Blanc C, Ruffer A. Multiphysics and energetic modeling of a vanadium redox flow battery. In: International Conference on Sustainable Energy Technologies (ICSET); October 2008; Singapore. Singapore: IEEE; 2008. pp. 759-764

[31] Sood V. HVDC transmission. In: Rashid M, editor. Power Electronic Handbook. 1st ed. Cambridge, UK: Academic Press; 2001. pp. 575-596

[32] Söder L, Ackermann T. Wind power in power systems: An introduction. In: Ackermann T, editor. Wind Power and Power System. 1st ed. New Jersey, USA: John Wiley and Sons Press; 2005. pp. 33-39. DOI: 10.1002/9781119941842.ch4

[33] Van der Hoven I. Power spectrum of horizontal wind speed in the frequency range from 0.0007 to 900 cycles per hour. Journal of Meteorology. 1956;**14**(2):160-164. DOI: 10.1175/1520-0469(1957)014<0160:PSOHWS>2.0.CO;2

[34] Matlab and Simulink Website. www.mathworks.com [Internet]. April 2016. Available from: http://www.mathworks.com/help/physmod/powersys/ref/synchronized12pulsegenerator.html [Accessed: April 2016]

[35] Kerdphol T, Qudaih Y, Hongesombut K, Watanabe M, Mitani Y. Intelligent determination of a battery energy storage system size and location based on rbf neural networks for microgrids. International Review of Electrical Engineering (IREE). 2016;**11**(1):78-87. DOI: 10.15866/iree.v11i1.7718

[36] Martinez M, Mercado P, Molina M. Determinación del Tamaño y Ubicación Óptimo de un Sistema de Almacenamiento de Energía en un Sistema de Potencia para Regulación Secundaria de Frecuencia. In: ERIAC/CIGRE, editor. Décimo Quinto Encuentro Regional Ibero-americano del CIGRÉ; May 2013; Foz de Iguazú, Brasil. Brasil: ERIAC/CIGRE; 2013. pp. 1-8

[37] Ontiveros L, Mercado P, Suvire G. A new model of the double-fed induction generator wind turbine. In: IEEE/PES, editor. Transmission and Distribution Conference and Exposition: Latin America (T&D-LA); November 2010; Sao Paulo, Brazil. Brazil: IEEE/PES; 2010. pp. 263-269

[38] Ontiveros L, Mercado P. Modeling of variable-speed wind farms for power systems dynamic studies. In: CIGRE/ERIAC, editor. Décimo Cuarto Encuentro Regional Ibero-americano de Cigré; May 2011; Ciudad del Este, Paraguay. Paraguay: CIGRE/ERIAC; 2011. pp. 1-8

[39] Silvestri G. Steam turbines. In: Elliot T, editor. Standard Handbook of Powerplant Engineering. 1st ed. New York, USA: McGraw-Hill Press; 1989. pp. 2.25-2.61. DOI: 10.1036/0070194351